Validation of a wind turbine gearbox strain simulation model in service to virtual sensing

Jelle Bosmans[0000-0002-9753-3043]1,2*, Matteo Kirchner[1,2], Jan Croes[1,2] and Wim Desmet[1,2]

[1*]Department of Mechanical Engineering, KU Leuven, Celestijnenlaan 300, Heverlee, B-3001, Belgium.
[2]DMMS Core lab, Flanders Make, Belgium.

*Corresponding author(s). E-mail(s): jelle.bosmans@kuleuven.be;

Abstract

Over the last decades, the use of wind power as a source of renewable power has increased, while the Levelized Cost of Electricity (LCoE) of wind power has fallen. In order to further drive down the LCoE, there is an increasing interest to monitor key turbine quantities in order to improve maintenance procedures and decrease downtime. In this paper, we focus on the indirect detection of one such key quantities, the torque load on the gearbox. In order to avoid expensive direct torque sensors, we study the potential of strain gauges installed on the gearbox housing as virtual torque sensors. Our results verify that the strain response is repeatable, torque-driven and predictable; which are the most important conditions for using the sensors in virtual load sensing. Next, we compare the measured strain response to simulated strain results obtained from a physics-based model. The model consists of a static FE model of the gearbox housing and a torsional model of the shafts and gears in the drivetrain. An optimisation approach selects the FE model node where the simulated strain best matches the measured strain. We conclude that the studied strain gauges are promising for model-based virtual sensing of the torque on the gearbox.

Keywords: strain measurements, model validation, gearbox, virtual sensing

1 Introduction

In 2020, renewable energy reached a share of 37% of electricity generation in the EU. Of this share, 36% was generated using wind power [1]. This share is expected to increase with ambitious goals set in the European Green Deal [2]. Meanwhile, the Levelized Cost of Electricity (LCoE) of wind power generation has dropped by 39% for onshore wind and 29% for offshore wind, over the last decade [3]. Three main contributors have enabled this cost reduction: firstly, the cost of new wind turbine installations has fallen [3]; secondly, the average size of wind turbines has increased, leading to more efficient aerodynamics, economies of scale, and higher capacity factors [4]; and finally, the unplanned downtime and associated production loss has been reduced trough reliability improvements [5].

In wind turbines with a geared drivetrain, improving reliability of the gearbox can contribute significantly to LCoE reductions, since gearbox repairs tend to have a high material- and time cost which contributes to maintenance cost and downtime [6, 7]. This is especially true for offshore turbines where maintenance operations have to deal with complex logistical chains and unpredictable weather conditions. In this context, there is an increasing interest to monitor key gearbox quantities with sensor networks. This information is used to shift the gearbox maintenance approach from reactive, periodic, or usage-based to predictive condition maintenance [4], with the ultimate goal of reducing the amount of unplanned downtime. Furthermore, monitored quantities can be used to close the loop from use- to design phase, improving the design within the current gearbox family or even serving as guidelines for new designs. Some of the most informative gearbox quantities to monitor are the operational loads (i.e. functional torque, bending moments, thrust and shear forces) since these loads are direct drivers for the consumption of fatigue life of gearbox components [5].

Operational loads can be measured directly with heavy duty sensor solution (e.g. HBM T12HT3 [8] for torque measurement), but such sensors are costly, intrusive, and their size conflicts with torque density targets. Hence these sensors are typically only used in lab situations and prototypes. Furthermore, to the authors' knowledge there are no direct load sensors on the market that can measure bending moments and forces on a rotating shaft. Virtual load sensing forms an alternative to avoid costly direct sensors. In virtual load sensing, indirect sensors with more favourable economics and placement conditions are used to infer the operational loads. The inference can be based on a model-based approach using a Kalman Filter [9–12], or on a data-based approach using machine learning [13].

For a sensor to be used in virtual load sensing, several conditions need to be met. Firstly, the sensor needs to show a load-driven response with sufficiently high signal-to-noise ratio. Secondly, the response should be repeatable, with a certain load condition and gearbox state leading to the same sensor output. If the model-based approach is used, it should also be possible to reliable predict the sensor output using a (physics-based) model. Finally, from a practical

point of view the sensor needs to be economic, and nonintrusive (i.e. no design changes should be necessary to accommodate for the sensor). In our case this implies that non-rotating sensors which are accessible on the exterior surface of the gearbox housing are preferred.

In this paper we study the potential of strain gauges installed on the housing of a wind turbine gearbox in the context of model-based virtual load sensing, based on measurements performed on an 850 kW wind turbine drivetrain. The gearbox is a three-stage gearbox with one planetary stage and two parallel gear stages. The focus of this paper is on the response of the strain gauges to varying levels of the torque load, the non-torque loads are outside the scope of this paper. A frequency range of interest from 0 to 10 Hz for the torque load was defined by the gearbox manufacturer.

First, we introduce the measurement campaign and the sensors that were used in Section 2. Next, we introduce a physics-based simulation model that can predict the strain on the housing in Section 3. Since the virtual sensor (which incorporates the model) will be used in a monitoring solution, particular attention is given to limiting the computational burden of the model. After these introductory sections, we discuss the analysis of the measurement data itself. First, a sensor response sensitivity study is performed to validate that the sensor response is load-driven and repeatable (Section 4). Next, a comparison is made between the measured strain and the simulated strain (Section 5). The observed discrepancies between the measurements and the simulation are discussed and an optimisation approach is introduced that can improve the match. The final outcome of this section is an assessment of the predictability of the sensor output. We wrap up with some concluding remarks in Section 6.

2 Measurement campaign and sensors

The measurement data considered in this paper was acquired during a measurement campaign conducted by the Center for Wind Power Drives, Aachen [14]. In this measurement campaign, an 850 kW wind turbine drivetrain was tested under various load conditions. The design of the test rig allows the drivetrain to be loaded with torsional and non-torque loads that are representative of real operating conditions. In the test campaign, the gearbox was extensively instrumented with strain gauges, temperature sensors, displacement probes, tachometers and accelerometers. A full description of the test campaign is not in the scope of this paper. However, a description of the design of the experiments can be found in [15] and a more extensive discussion of all sensors used in the campaign will be available in a forthcoming publication [16].

In this paper the focus is on two specific segment of the measurement data. In the first segment, the gearbox is loaded with a slowly varying torque ramp while the rotation speed is kept constant. We analyse this segment in Section 4 to perform a sensitivity study of the strain response versus the torque load. In the second segment, a constant speed and torque are applied to the gearbox. We use this segment to compare the simulated strain response to the measured

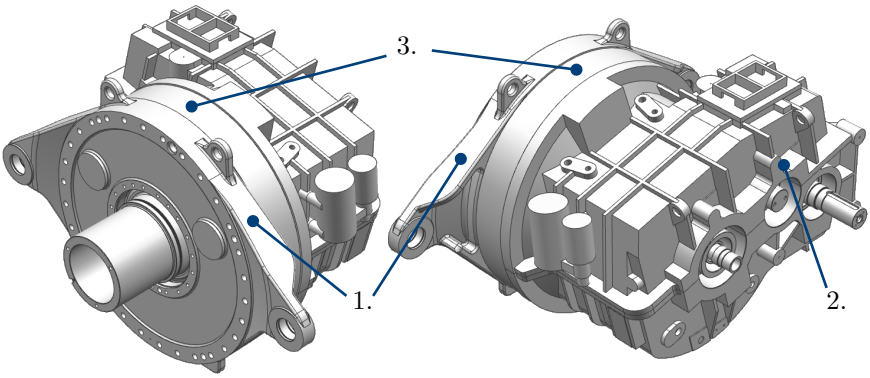


Fig. 1 CAD model of the gearbox showing strain gauge positions on the torque arm (1.), bearing seat (2.), and ring gear (3.).

response in Section 5. During both segments the non-torque loads are kept constant.

Three main groups of strain gauges located at key points on the gearbox housing (see Figure 1) are analysed in this paper. The analysis will focus on the results of one representative strain gauge from each group:

1. on the Torque Arm (TA) which forms the main connection point of the gearbox to the nacelle mainframe,
2. on the bearing seat for the parallel stages on the high-speed side of the gearbox,
3. on the outside surface of the Ring Gear (RG) of the planetary stage.

These strain gauge positions were chosen since they are expected to yield a predictable load-driven strain response. Furthermore, all strain gauges are accessible on the external surfaces of the gearbox. Next to the strain gauges, a torque sensor on the main shaft is used for validation purposes. The tachometer on the main shaft completes the measurement set. The speed signal from the tachometer can be integrated and combined with a single pulse per rotation reference sensor to construct a measurement of the absolute angle of the planet carrier.

3 Strain simulation model

To be used in virtual load sensing, the strain simulation model must be able to predict the strain output from the strain gauges used in the measurement campaign. Furthermore, the computational burden of the model should be limited to allow real-time execution of the virtual load sensor in a monitoring solution. A model of the drivetrain and gearbox that fulfils these requirements was introduced by the authors in [9]. As such, we will only briefly discuss the properties of the drivetrain and gearbox model in 3.1, as they were introduced in [9]. Next, we introduce a continued development of the strain calculation methods in 3.2.

3.1 Drivetrain and gearbox housing model

A schematic overview of the drivetrain and gearbox housing model is given in Figure 2. The model consists of two main components indicated as two columns in the scheme. The first component is a Finite Element (FE) model of the gearbox housing, including all structural (non-rotating) components. Since the FE model has a large number of degrees of freedom, model reduction is applied to limit the computation time. The model reduction starts by performing static test simulation with test loads ($\mathbf{F}_{\text{test}}$) applied in different directions at the bearing locations and at several points along the width and circumference of the ring gear. A strain response matrix is constructed by multiplying the resulting strain at the sensor locations with the inverse of the applied load. By selecting the relevant columns from the part of the response matrix related to the ring gear forces, an angle dependent response matrix $\mathbf{S}\left(\theta_{\text{PC}}\right)$ is constructed which describes the response of each strain output location to the forces applied by the gears and bearings on the housing. This matrix depends on the planet carrier angle θ_{PC} since this angle determines the force path from the planets to the ring gear and the housing.

Next to the FE model, a torsional drivetrain model describes the torsional dynamics of all shafts and gears in the drivetrain using discrete inertia and stiffness elements. This model also calculates the resulting gear and bearing forces. The gear force $\mathbf{F}_{\text{gear}}$ is represented as a single force vector applied at the pitch point along the line of action, for the planetary stage the location of the pitch points for the different planet-ring contacts depends on θ_{PC}. The bearing forces $\mathbf{F}_{\text{bearing}}$ are calculated by assuming quasi-static equilibrium of the gear-shaft-bearing system. The forces applied to the ring gear $\mathbf{F}_{\text{RG}}$ are concatenated with the bearing forces to form the complete force vector $\mathbf{F}$. By assuming linear static behaviour, this vector can be multiplied by the response matrix to calculate the strain in a given load condition through superposition.

The assumption of linear behaviour is motivated by an earlier study by the author which found that the gearbox has no flexible eigenmodes in the frequency range of interest for this study [17]. Furthermore, the non-linear effects in the gearbox (e.g. variable transmission error of a gear pair) are also limited to frequencies above this range. Finally, non-linear contact effects in gears and bearings have a rather localized effect on the strain field. As such, the model can still be expected to predict the strain output from a sensor with reasonable accuracy, so long as the sensor is sufficiently far from the contact zones.

3.2 Strain output prediction

While the previous section discussed how to simulate strain on the gearbox housing in a computationally efficient way, it did not consider that the strain output should accurately represents the physical strain gauge. Two aspects must be addressed to make this step. Firstly, the post-processing steps necessary to convert the 3D strain tensor resulting from the FE model simulation

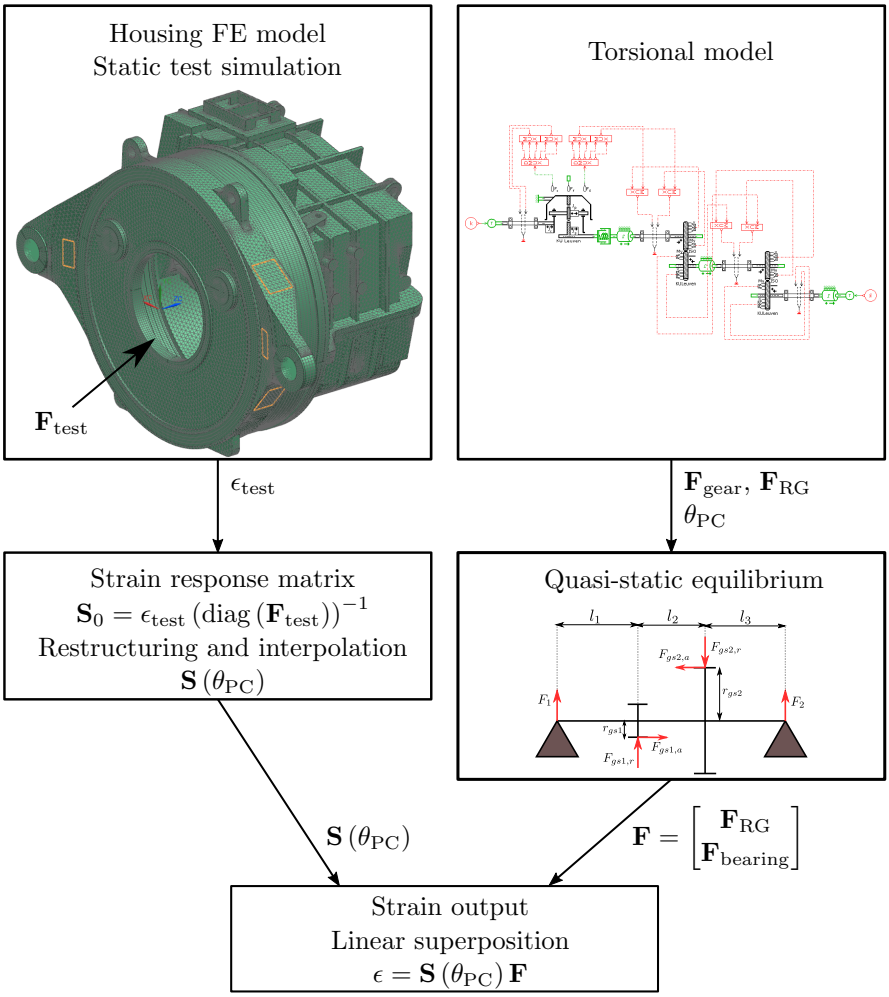


Fig. 2 Schematic overview of the wind turbine drivetrain and -gearbox simulation model [9].

to a representative uni-axial strain in the direction of the strain gauge are defined. Secondly, an the output node in the FE model which best represents the physical strain gauge is selected.

The post-processing of the 3D strain tensor ϵ from the FE model happens in two steps. The first step is an averaging step, which calculates the strain at a certain node as the average strain output of all connected elements. This averaging reflects the fact that a strain gauge has a finite surface area and actually measures average strain over this area, rather than at a single point (or node). The element size within the strain gauge patches has also been chosen to reflect the size of the strain gauges used. In the second step, a coordinate

transformation is applied to the strain tensor,

$$\tilde{\boldsymbol{\epsilon}} = R^{\top} \boldsymbol{\epsilon} R := \begin{bmatrix} \tilde{\epsilon}_{11} & \tilde{\epsilon}_{12} & \tilde{\epsilon}_{13} \\ \tilde{\epsilon}_{21} & \tilde{\epsilon}_{22} & \tilde{\epsilon}_{23} \\ \tilde{\epsilon}_{31} & \tilde{\epsilon}_{32} & \tilde{\epsilon}_{33} \end{bmatrix}, \tag{1}$$

where R is a coordinate transformation matrix defined as follows:

$$R = \left[\vec{n}_{\mathrm{SG}} \ \left(\vec{n}_{\mathrm{SG}} \times \vec{n}_{\mathrm{Surf}} \right) \ \vec{n}_{\mathrm{Surf}} \right], \tag{2}$$

where $\vec{n}_{\mathrm{SG}}$ is a vector that is aligned with the strain gauge, and $\vec{n}_{\mathrm{Surf}}$ is a vector normal to the surface where the strain gauge is installed. By applying this transformation, the strain output from the strain gauge is predicted by $\tilde{\epsilon}_{11}$. The normal plane strain state is described by the upper left 2-by-2 block matrix of $\tilde{\boldsymbol{\epsilon}}$, this is useful in case strain is measured in multiple directions by a rosette. Since all post-processing steps are linear operations, they can be included directly in the calculation of the strain response matrix $\mathbf{S}\left(\theta_{\mathrm{PC}}\right)$.

As noted by [18], the definition of an FE model output node that best represents the physical strain gauge is complicated by geometrical and measurement errors. Geometrical errors exist because the FE model does not exactly represent the geometry of the gearbox housing due to geometry simplification in the FE model (e.g. the removal of rounded edges or chamfers) and manufacturing tolerances. The latter is particularly significant for large cast iron parts such as the TA [19]. Measurement errors here refer to errors made when measuring the position of the physical strain gauge and using that information to find a matching node in the FE model. Next to the limited accuracy of dimensional measurement tools, the presence of geometrical errors and simplifications further complicates measuring the position of the strain gauges, as reference geometry (e.g. edges, corner points) which exists on the physical housing might not be represented in the FE model. As a solution, strain gauge positions are not defined as a single node, but rather as a patch of plausible candidate nodes around the nominal position of the strain gauge. Several such patches are highlighted in the FE model in the top left corner of Figure 2 as orange rectangles. An optimisation will select the node corresponding to the best matching strain gauge position (see Section 5).

4 Strain response sensitivity study

In this section, we analyse the strain measurements considering measurement data from a test where a slowly varying torque is applied to the drivetrain at constant speed. While this test does not represent realistic operating conditions, it does allow us to study the sensor response at varying torque levels without other influencing factors. The aim of this analysis is to verify whether the strain response complies to the following conditions:

1. the strain response is linear with respect to the torque load T,

2. the strain response depends periodically on the planet carrier angle θ_{PC},
3. the strain response can be represented as

$$\epsilon\left(T, \theta_{\mathrm{PC}}\right) = f_T T f_\theta\left(\theta_{\mathrm{PC}}\right) + d, \tag{3}$$

where f_T is a constant factor describing torque sensitivity, $f_\theta\left(\theta_{\mathrm{PC}}\right)$ is a periodic function with period 360°, and d is a constant factor that models constant offsets in the response.

If and only if these conditions are met, the strain response model can be expected to accurately predict the measured strain since the model explicitly assumes linearity. In order to validate these conditions, the measured data is reformatted as a 3D point cloud with coordinates $\left[T \mod\left(\theta_{\mathrm{PC}}, 360°\right)\ \epsilon\right]$. Next, a surface of the form defined in Eq. 3 is fitted to the data. If the resulting fit is of high quality, the conditions above can be considered satisfied. To evaluate the quality of a fit, the Root Mean Square Error (RMSE) and the adjusted coefficient of determination $\bar{R}^2$ are used as metrics. The RMSE measures the quality of the fit only in terms of the deviation between the fitted surface and the data. $\bar{R}^2$ is a normalised metric that describes the proportion of the variation in the measured strain that is predictable from the fitting parameters. $\bar{R}^2$ also includes a correction that increases with the amount of fitted parameters, as a result it can be used as a metric to detect over-fitting.

The remainder of this section will discuss the surface fit results of the strain gauge groups listed in Section 2. For each strain gauge group, an appropriate function $f_\theta\left(\theta_{\mathrm{PC}}\right)$ is defined. These functions are chosen by visually inspecting the strain response and choosing a fitting mathematical function. As such, the choice of fitting function remains rather arbitrary. A more rigorous approach could be defined by comparing the quality of fit (RMSE and $\bar{R}^2$) for different fitting functions.

4.1 Results for torque arm strain gauges

The strain response on the torque arm is characterised by a (0Hz) offset with a ripple, both the offset- and the ripple magnitude increase with the torque (see Figure 6). The strain offset is explained by the reaction torque of the gearbox due to the torque reduction, which is the major loading mechanism for the torque arm. The ripple is caused by the varying force path of gear forces from the planetary stage through the housing as the planet carrier rotates. Because there are three planets in the planetary stage, the ripple has a period of 120° with respect to θ_{PC}. This response can be described with an equation containing a linear term for the torque dependency and a Fourier series approximation for the angle dependency, following the form defined in Eq. 3:

$$\epsilon\left(T, \theta_{\mathrm{PC}}\right) = T \underbrace{\left[a_0 + \sum_{n=1}^{N} a_n \cos\left(n\omega\theta_{\mathrm{PC}}\right) + b_n \sin\left(n\omega\theta_{\mathrm{PC}}\right)\right]}_{f_\theta\left(\theta_{\mathrm{PC}}\right)} + d, \tag{4}$$

Table 1 Surface fitting quality metrics and parameters for the response study for strain gauges on the torque arm and bearing seat.

Strain gauge group	$\bar{R}^2$	RMSE $\frac{\mu m}{m}$	ω	a_n $\frac{\mu m}{m}$kNm^{-1}		b_n $\frac{\mu m}{m}$kNm^{-1}		d $\frac{\mu m}{m}$
Torque arm	0.949	6.083	3.013	a_0	0.214	b_1	−0.004	7.947
				a_1	0.043	b_2	0.019	
				a_2	0.015	b_3	0.008	
				a_3	−0.007			
Bearing seat	0.989	3.225	3.029	a_0	0.261	b_1	0.001	10.033
				a_1	0.000			

where ω, $a_{0\ldots N}$, and $b_{1\ldots N}$ are the surface fit parameters and N is the order of the Fourier series. In this equation and all following equations, θ_{PC} is expressed in degrees and the trigonometric functions use degrees rather than radians.

Figure 3 shows the measured data as well as the fitted surface and Table 1 shows the fit quality metrics and parameters. The surface fit parameters were calculated using the Matlab Curve Fitting Toolbox, which uses non-linear least-squares optimisation to calculate the best fitting parameters. The order N was set to 3 for this analysis, as this setting leads to a good fitting result. Further increasing N does not significantly improve the RMSE or $\bar{R}^2$ and the fitted parameters become insignificantly small for the higher order terms.

The fitted surface shows an excellent match with the measured data, with a high $\bar{R}^2$ and an RMSE value that is small when compared to the magnitude of the strain response. The fitted parameters confirm that the strain ripple has a period of 120° since $\omega \approx 3$. Furthermore, observe that the linear torque dependency (a_0) has the largest contribution, and the Fourier terms have a smaller contribution which also decreases for higher order terms. Since the surface fit is of high quality, we can conclude that this strain sensor meets the conditions specified at the start of this section.

4.2 Results for bearing seat strain gauges

The strain response on the bearing seats is very similar to the response on the torque arms, but the magnitude of the ripple is much less pronounced (see Figure 7). Hence, Eq. 4 can be used as surface fitting equation for this data. Figure 4 shows the measured data as well as the fitted surface and the lower half of Table 1 shows the fit quality metrics and parameters. The order N was decreased to 1 for this analysis, based on similar reasoning as outlined above.

Similar to the results for the TA strain gauges, the fitted surface shows an excellent match with the measured data. Because of the smaller magnitude of the torque ripple, the linear torque dependency is an even more dominant factor in the response and the Fourier terms have a small contribution. This strain sensor also meets the conditions specified at the start of the section.

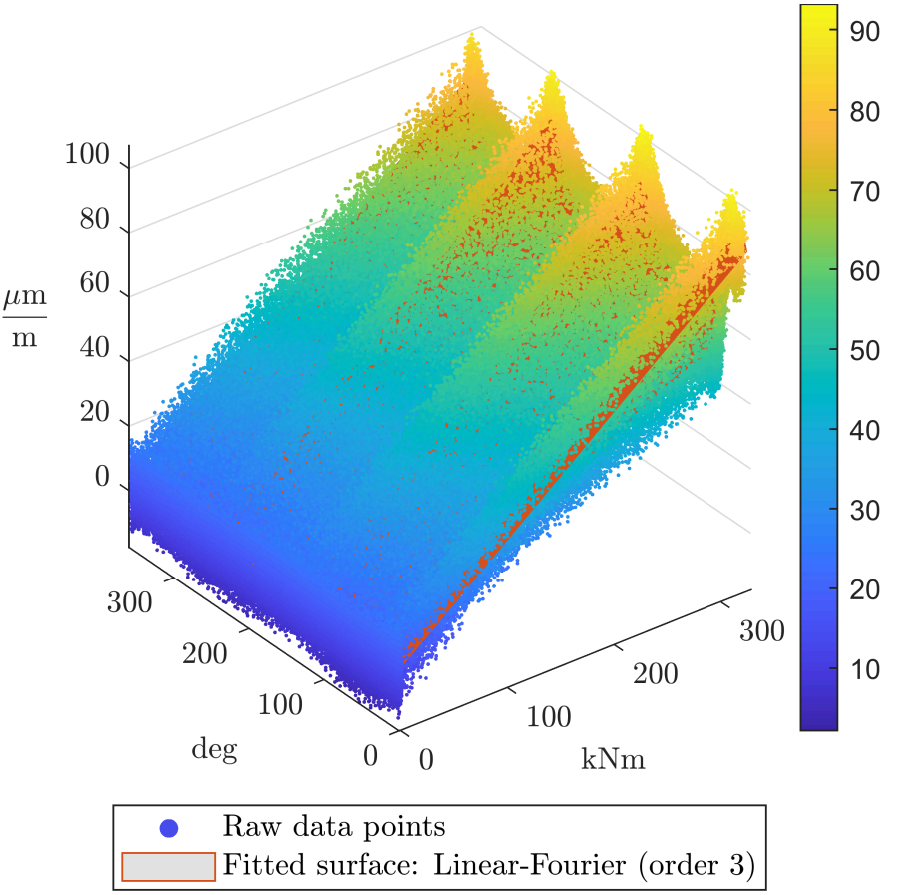


Fig. 3 Results of strain response study for strain gauges on the torque arm.

4.3 Results for ring gear strain gauges

The strain response on the external surface of the ring gear is significantly different from the previous two locations. The strain response on the ring gear shows three peaks associated with a planet gear passing the location of the sensor, i.e. spaced 120° apart with respect to θ_{PC} (see Figure 8). The height of the peak increases with the applied torque. Between the peaks the strain response is close to zero. Such a response can be described mathematically as:

$$\epsilon\left(T,\theta_{\mathrm{PC}}\right) = T \underbrace{\sum_{n=0}^{2} a \exp\left(-\left[\frac{\theta_{\mathrm{PC}} - b - n \times 120^{\circ}}{c}\right]^{2}\right)}_{f_{\theta}(\theta_{\mathrm{PC}})} + d, \tag{5}$$

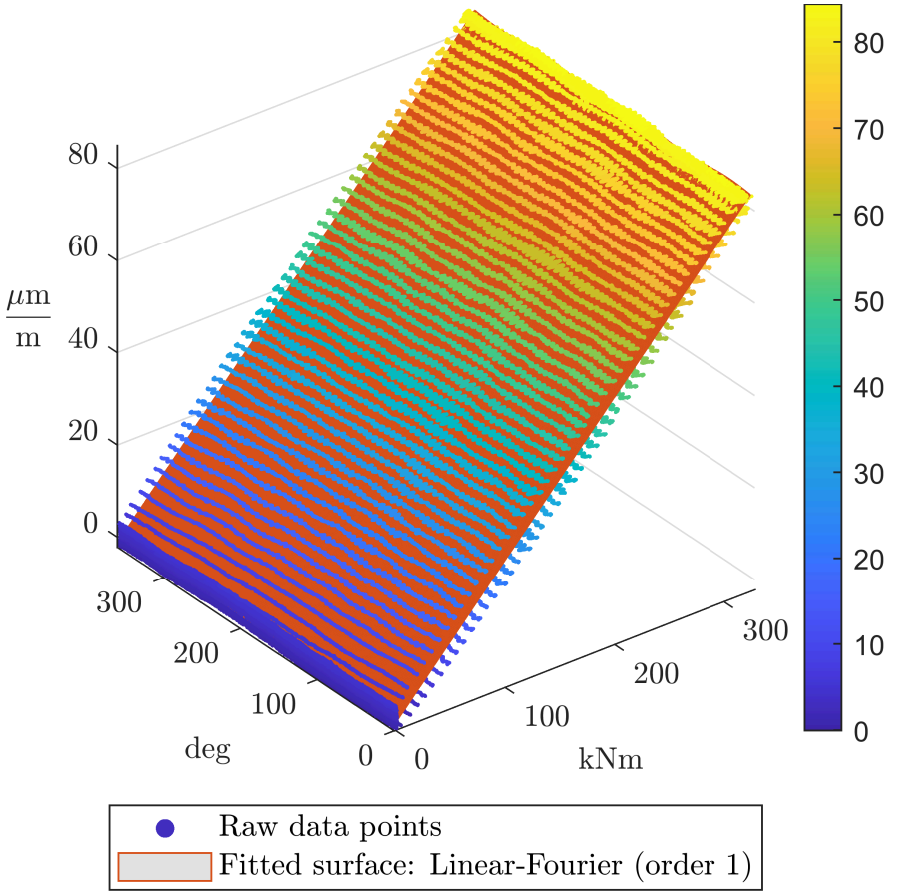


Fig. 4 Results of strain response study for strain gauges on the bearing seats of the high-speed stage of the gearbox.

where a, b, c, and d are the surface fit parameters which control the height of the peaks; the (angular) location of the first peak; the width of the peaks; and the constant offset, respectively. This function is inspired by the probability density function of a Gaussian distribution manipulated to have multiple peaks. Note that the function description is only valid for $\theta_{\mathrm{PC}} \in [0°, 360°]$.

Figure 5 shows the measured data as well as the fitted surface and Table 2 shows the fit quality metrics and parameters. Similar to the previous results, the fitted surface shows an excellent match with the measured data. This strain response has the highest linear sensitivity to torque (a) of all strain gauge groups. Like the other strain gauge groups, the response of this sensor meets the conditions specified at the start of the section.

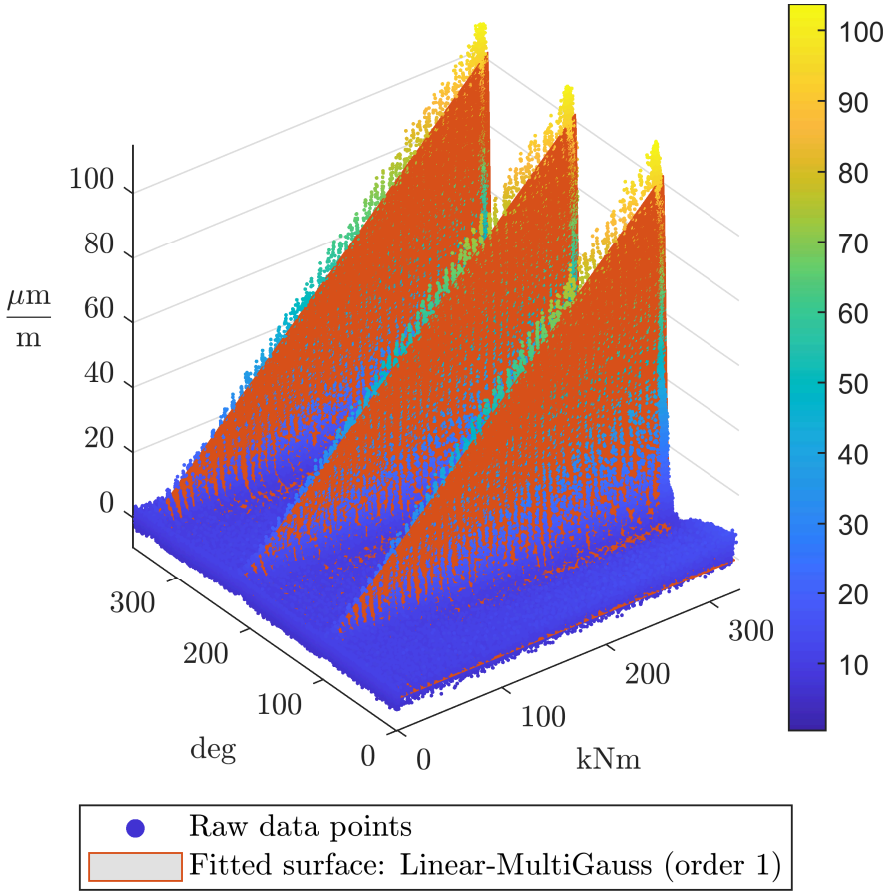


Fig. 5 Results of strain response study for strain gauges on the ring gear.

Table 2 Surface fitting quality metrics and parameters for the response study for strain gauges on the ring gear

Strain gauge group	$\bar{R}^2$	RMSE $\frac{\mu m}{m}$	a $\frac{\mu m}{m}\text{kNm}^{-1}$	b deg	c deg^{-1}	d $\frac{\mu m}{m}$
Ring Gear	0.948	3.598	0.319	99.329	5.109	−0.8345

5 Correlation of strain measurements to simulation

In this section, we investigate the correlation of the measured strain to simulation results from the model introduced in Section 3. The measured strain is taken from a measurement where the speed and torque are kept constant at 20 RPM, and 300 kNm, respectively . These conditions are reproduced in

the model by applying the same torque and speed. Furthermore, the viscous damping factors in the torsional model are tuned so the resulting energy loss matches the measured efficiency of the gearbox.

As mentioned in Section 3.2, the selection of an output node in the FE model that represents the physical strain gauge position presents some challenges. An optimisation approach is used that selects the output node by minimizing the Root Mean Square Error (RMSE) between simulated and measured strain. Only output nodes within the candidate node patch for a given strain gauge are considered (see Section 3.2 and Figure 2).

Figures 6-8 show a comparison between the measured strain, the simulated strain at the nominal strain gauge position, and at the optimised position. The data in these graphs covers approximately two full rotations of the planetary stage. Table 3 shows a comparison between the same signals based on several statistical properties.

For the torque arm strain gauge (Figure 6), the simulated strain at the nominal position already shows quite a good match to the measurement, both visually and in terms of RMSE and mean strain $\bar{\epsilon}$. These metrics are further improved with the strain gauge position optimisation. The magnitude of the ripple on the strain signal can be quantified with the range and Inter Decile Range (IDR) of the strain signal. The range is sensitive to noise and outliers and for this particular signal the noise level is relatively high compared to the magnitude of the ripple (this effect could be countered by applying a low-pass filter). The IDR is less sensitive to outliers and the IDR of measurement and simulation is in moderately good agreement, with a small improvement made after optimizing the strain gauge position. The normalised distance $\bar{d}$ measures the distance between the nominal- and the optimised strain gauge position, divided by the size of the strain gauge. For this strain gauge, $\bar{d} = 1.9$, which is relatively large. However due to the complex geometry of the torque arm with many rounded edges it is plausible that the nominal strain gauge position was not measured very accurately. The remaining RMSE after optimizing the strain gauge position is low compared to the magnitude of the strain response and the noise level in the measured signal, hence we conclude that the response of this sensor can be predicted reliably using the strain simulation model.

For the bearing seat strain gauge (Figure 7), the simulated strain at the nominal position shows a large offset in $\bar{\epsilon}$, with a correspondingly high RMSE. This offset is removed to a large degree when the position is optimised, also decreasing the RMSE. Notice that this improvement is achieved with a relatively small change in the position of the strain gauge. This implies that a large strain gradient exists on the bearing seat, due to complex geometry and the local load of the bearing force. The range and IDR are less relevant for this position because of the small size of the ripple. After the strain gauge position is optimised, the remaining RMSE is still larger than for the TA strain gauges because the model still overestimates the strain response. This could still be improved by refining the mesh size in the bearing seat area to capture the strain gradient more accurately. Another possible explanation for the

overestimation of the strain response is that some covers in the vicinity of the bearing were not included in the FE model, these components might have a stiffening effect that would lead to a lower strain response. Alternatively, an empirical correction factor can be applied to the strain to improve the match simulations and measurements. Since the strain response scales linearly with the torque, the correction factor will also be linear.

Finally, for the ring gear strain gauge (Figure 8), the nominal position already yields the best match in the strain simulation results. The simple cylindrical geometry of the ring gear probably allowed for a more accurate position measurement of this strain gauge, making further adjustments unnecessary. The nature of the strain signal with sharp peaks and low strain levels in between peaks makes a comparison of $\bar{\epsilon}$ less relevant. Instead the range of the strain response is considered as a representative measure of the height of the peaks. The model overestimates the strain peak (see maginification in Figure 9) due to the assumptions of the model, which represent the force applied by the planets on the ring gear as a single point load while in fact there exists a distributed contact load over the flank width of the teeth in contact. In order improve the prediction of the model for the strain gauges on the ring gear, the distributed contact force should be taken into account, but this increases the computational burden of the model. Just like for the bearing seat strain gauges, an alternative is the application of a correction factor to improve the match simulations and measurements. Note that due to Saint-Venant's principle the strain far away from the ring gear (e.g. on the torque arm) will not be influenced significantly by the contact force model, as long as the forces are statically equivalent, hence the better correlation for these signals.

6 Conclusions

In this paper, we studied the potential of strain gauges installed on the housing of a wind turbine gearbox in the context of model-based virtual load sensing for indirect monitoring of wind turbine gearbox loads. We analysed measurements performed on an 850kW wind turbine drivetrain including a heavily instrumented gearbox. The analysis is focussed on the response of the different sensors versus torque. The gearbox under study is a three-stage gearbox with one planetary stage and two parallel gear stages. We studied the response of three strain gauges located on external surface of the gearbox housing: on the Torque Arm (TA) which forms the main connection point of the gearbox to the turbine mainframe, on the bearing seat for the parallel stages on the high-speed side of the gearbox, and on the surface of the Ring Gear (RG) of the planetary stage.

We studied the response of the strain gauges at different torque levels by analysing data from a test where a slowly varying torque was applied to the gearbox at constant speed. In this analysis, we verified that the strain response increases linearly with the applied torque T and that it has a periodic dependency on the planet carrier angle θ_{PC}. These conditions were verified

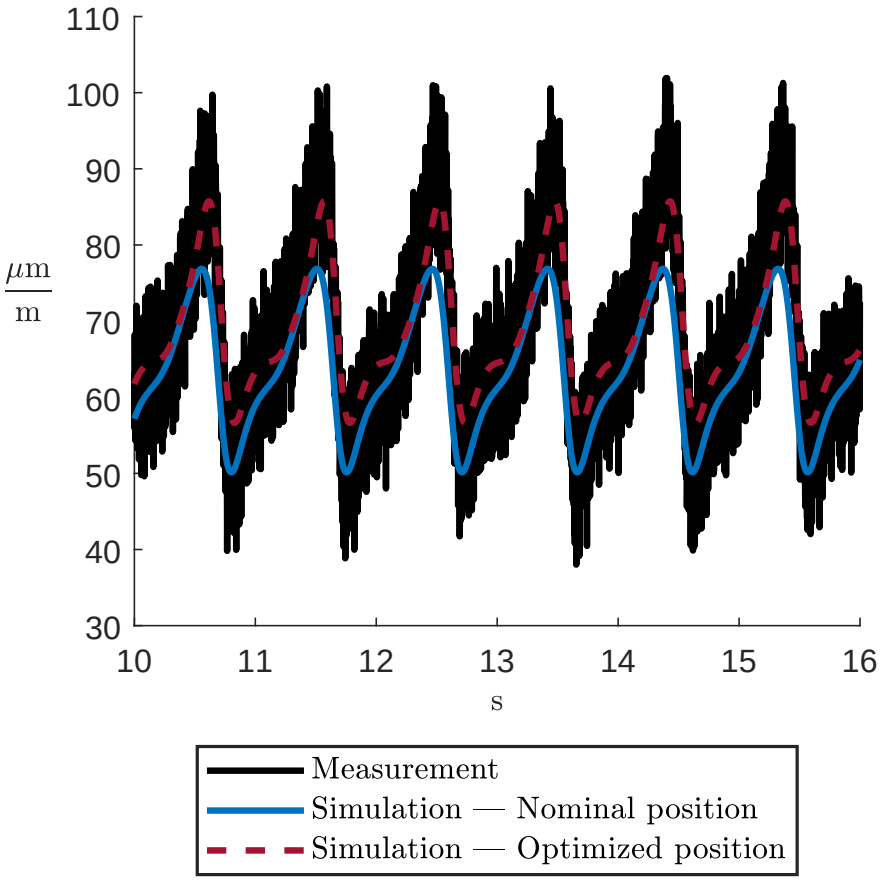


Fig. 6 Comparison of measured and simulated strain on the torque arm.

by fitting a surface through the measured data points, the parametrisation of the surface is chosen so that it meets the conditions. Since for each of the strain gauge locations, a high quality fit was achieved we conclude that the strain response meets the conditions. This is an important condition for using the strain gauges in a model-based virtual load sensing solution, since the strain response needs to be repeatable, load-driven and predictable for this application.

Next, we compared the measured strain response to simulated strain results obtained from a physics-based model. The model consists of a static FE model of the gearbox housing and a torsional model of the shafts and gears in the drivetrain. An optimisation approach was introduced to select the node in the FE model where the simulated strain best matches the measured strain. We showed that for the strain gauges on the TA, the response of the sensor can be predicted reliably by the simulation model. For the strain gauges on the bearing seat, a significant offset in the response was observed. While the offset can be reduced to a great degree by optimising the sensor position, a

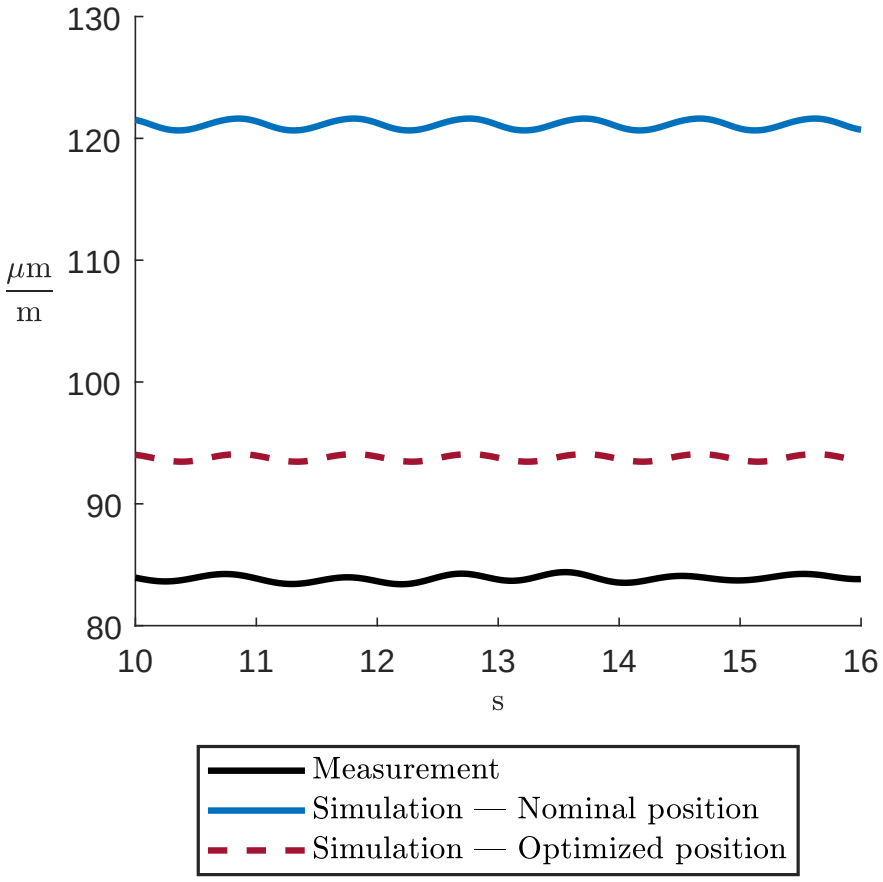


Fig. 7 Comparison of measured and simulated strain on the bearing seat.

small offset remains. This offset could be decreased further by refining the FE model mesh at the sensor location or by applying an empirical correction factor to this measurement. The required correction factor can be derived directly from the presented analysis. The correction will scale linearly with the applied torque since the linearity of the response was shown in the strain response study. Finally for the strain gauges on the ring gear, we observe that the simulation model overestimates the peak strain that occurs when a planet gear passes near the sensor. This is due to the assumptions in the model, which represent the force applied by the planets on the ring gear as a single point load. Relaxing this assumption or applying a correction factor could improve the match between the simulated- and the measured strain.

Our analyses indicate that the studied strain gauges are promising for model-based virtual sensing of the torque on the gearbox. While some mismatch between the simulated strain and the measurements remains even after optimisation, it should be noted that many estimation algorithms (e.g Kalman

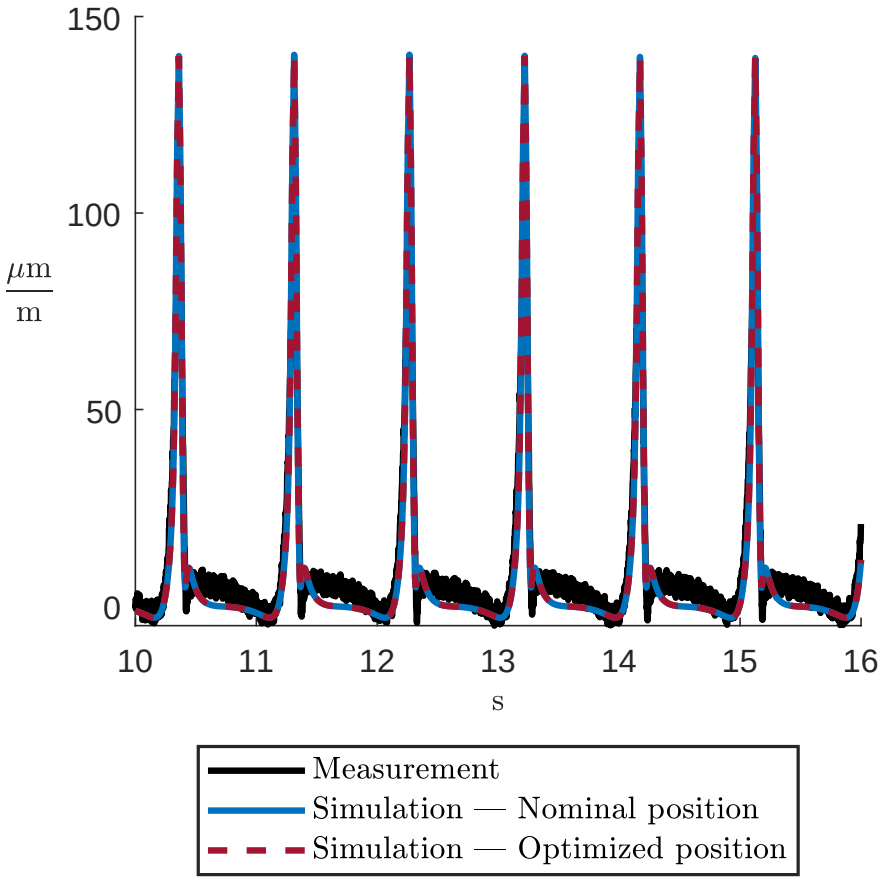


Fig. 8 Comparison of measured and simulated strain on the ring gear.

Filtering) used in virtual sensing explicitly account for errors and noise in the measurements. So even if a closer match between the measured and simulated strain is not feasible or not desirable (for example because of higher model complexity), accurate virtual torque sensing performance can still be achieved. The investigation of virtual torque sensing based on the presented model and sensors forms a next step for the research.

In other future analysis, the response of the sensors under more dynamically varying speed and torque profiles should be studied, since the torque ramp at constant speed does not represent realistic operating conditions. Since the sensor response study is performed in the angular domain, no changes are necessary to the methodology to allow for varying speed. The presented model can be expected to predict the strain accurately for varying speed and torque profiles if the input does not excite eigenmodes in the gearbox, and if the varying speed and torque is tracked in the model. The former condition is satisfied since an earlier study validated that the gearbox has no eigenmodes

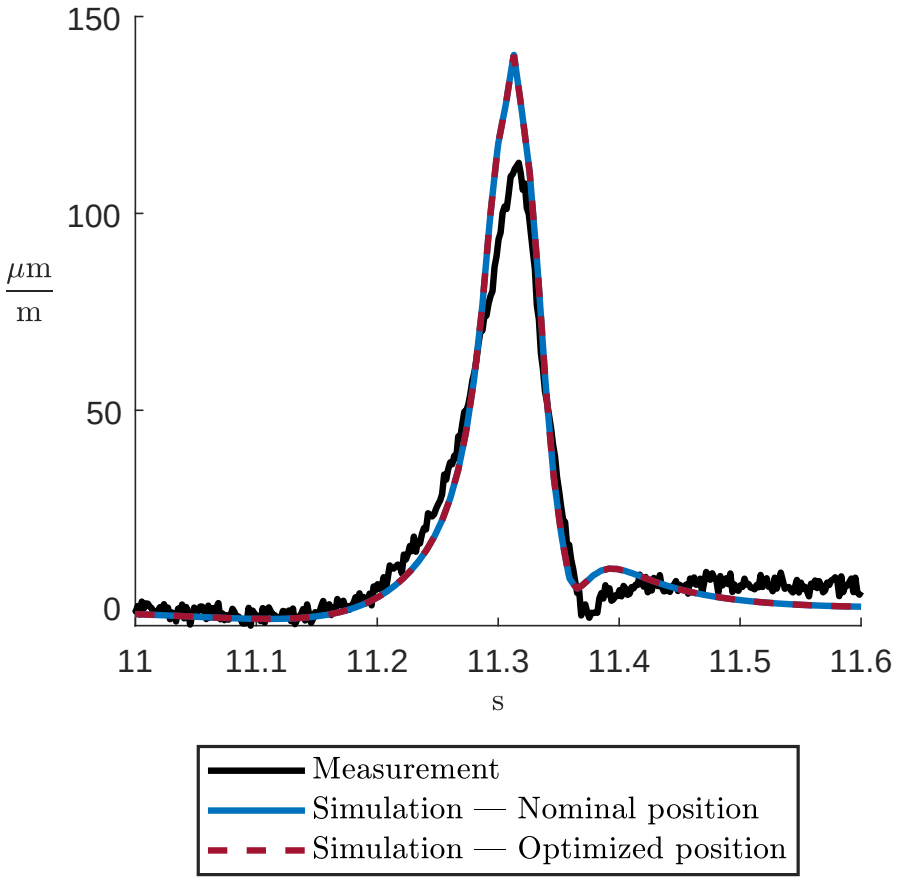


Fig. 9 Comparison of measured and simulated strain on the torque arm, magnified to focus on a single strain peak.

in the frequency range of interest (0 to 10Hz). The latter condition is satisfied by using an iterative estimation algorithm which corrects the speed and torque based on the measured values.

Finally, also the non-torque load on the gearbox will be considered in future research. This analysis will follow a similar approach as presented in this paper. As a first step, a sensor response sensitivity study will be performed based on dedicated measurement runs where a single non-torque load is varied while the other loads are kept constant. Next, the non-torque loads will be included in the current model by adding the non-torque loads to the quasi-static equilibrium equations of the main shaft. The simulated strain will then be compared to the measured strain in order to validate the model. In case the model accuracy is not satisfactory, a more accurate representation of the non-torque loads can be included by using a more sophisticated modelling strategy such as multibody modelling, but this comes with the downside of a higher computational cost.

Table 3 Correlation results between measured and simulated strain response, showing Root Mean Square Error (RMSE), mean strain value ($\bar{\epsilon}$), range of the strain signal (range(ϵ)), Inter Decile Range (IDR(ϵ)), and the distance between the optimised strain gauge position and the nominal position divided by the strain gauge size ($\bar{d}$).

Strain gauge group	Signal type	RMSE $\frac{\mu m}{m}$	$\bar{\epsilon}$ $\frac{\mu m}{m}$	range(ϵ) $\frac{\mu m}{m}$	IDR(ϵ) $\frac{\mu m}{m}$	$\bar{d}$
Torque arm	Measured		68.3	63.9	34.6	
	Simulated nominal position	8.9	63.6	26.7	23.6	
	Simulated optimised position	6.7	68.6	29.1	24.5	1.9
Bearing seat	Measured		83.9	1.0	0.7	
	Simulated nominal position	37.5	121.1	1.0	0.9	
	Simulated optimised position	10.1	93.8	0.6	0.6	0.7
Ring gear	Measured		10.2	101.0	30.6	
	Simulated nominal position	12.8	8.5	147.8	23.1	
	Simulated optimised position	12.8	8.5	147.8	23.1	0

Acknowledgments. This research is supported by the Flanders Innovation & Entrepreneurship Agency within the V6LoadS project in cooperation with the Center for Wind Power Drives and ZF Wind Power. The Center for Wind Power Drives is acknowledged for providing the measurement data considered in this paper, in the context of the joint V6LoadS project. Furthermore, the Research Fund KU Leuven is gratefully acknowledged for its support.

References

[1] Eurostat. Renewable energy on the rise: 37% of EU's electricity (2022). URL https://ec.europa.eu/eurostat/web/products-eurostat-news/-/ddn-20220126-1.

[2] A European Green Deal (2019). URL https://commission.europa.eu/strategy-and-policy/priorities-2019-2024/european-green-deal{_}en.

[3] IRENA. Renewable Power Generation Costs in 2019. Tech. Rep., IRENA, Abu Dhabi (2020). URL https://www.irena.org/-/media/Files/IRENA/Agency/Publication/2018/Jan/IRENA{_}2017{_}Power{_}Costs{_}2018.pdf. arXiv:1011.1669v3.

[4] Nejad, A. R. *et al.* Wind turbine drivetrains: State-of-the-art technologies and future development trends. *Wind Energy Science* **7** (1), 387–411 (2022). https://doi.org/10.5194/wes-7-387-2022 .

[5] Peeters, J., Schmidt, S. & Verellen, M. Desmet, W., Pluymers, B., Moens, D. & Neeckx, S. (eds) *Empowering a sustainable future with continuous innovation in wind turbine powertrains.* (eds Desmet, W., Pluymers, B., Moens, D. & Neeckx, S.) *Proceedings of ISMA2022 International Conference on Noise and Vibration Engineering*, 27–39 (KU Leuven, Leuven, 2022).

[6] Turnbull, A., McKinnon, C., Carrol, J. & McDonald, A. On the Development of Offshore Wind Turbine Technology: An Assessment of Reliability Rates and Fault Detection Methods in a Changing Market. *Energies* **15** (9) (2022). https://doi.org/10.3390/en15093180 .

[7] Carroll, J., McDonald, A. & McMillan, D. Failure rate, repair time and unscheduled O&M cost analysis of offshore wind turbines. *Wind Energy* **19**, 1107–1119 (2016). URL http://doi.wiley.com/10.1002/we.1887. https://doi.org/10.1002/we.1887 .

[8] HBM. T12HT - Very High-Capacity Torque. URL https://www.hbm.com/en/6337/t12ht-high-capacity-torque-sensor.

[9] Cappelle, C. *et al.* Sensor selection for cost-effective virtual torque measurements on a wind turbine gearbox. *Forschung im Ingenieurwesen/Engineering Research* **85** (2), 325–334 (2021). https://doi.org/10.1007/s10010-021-00464-z .

[10] Forrier, B., Naets, F. & Desmet, W. Broadband load torque estimation in mechatronic powertrains using nonlinear kalman filtering. *IEEE Transactions on Industrial Electronics* **65** (3), 2378–2387 (2017). https://doi.org/10.1109/TIE.2017.2739709 .

[11] Perišić, N., Kirkegaard, P. H. & Pedersen, B. J. Cost-effective shaft torque observer for condition monitoring of wind turbines. *Wind Energy* **18**, 1–19 (2015). https://doi.org/10.1002/we .

[12] Mehlan, F. C., Nejad, A. R. & Gao, Z. Digital twin based virtual sensor for online fatigue damage monitoring in offshore wind turbine drivetrains. *Journal of Offshore Mechanics and Arctic Engineering* **144** (December), 1–9 (2022). https://doi.org/10.1115/1.4055551 .

[13] Azzam, B., Schelenz, R. & Jacobs, G. Sensor Screening Methodology for Virtually Sensing Transmission Input Loads of a Wind Turbine Using Machine Learning Techniques and Drivetrain Simulations. *Sensors* **22** (10) (2022). https://doi.org/10.3390/s22103659 .

[14] CWD. Center for Wind Power Drives. URL www.cwd.rwth-aachen.de.

[15] Azzam, B., Schelenz, R., Cardaun, M. & Jacobs, G. From Simulations to Accelerated Testing: Design of Experiments for Accelerated Load Testing of a Wind Turbine Drivetrain Based on Aeroelastic Multibody Simulation Data. *Applied Sciences* **13** (1), 356 (2023). https://doi.org/10.3390/app13010356 .

[16] Azzam, B., Schelenz, R. & Jacobs, G. Development of a virtual sensor to estimate wind turbine gearbox input loads [Unpublished manuscript] .

[17] Bosmans, J., Gallas, S., Rocha de Melo Filho, N. G., Kirchner, M. & Desmet, W. Desmet, W., Pluymes, B., Moens, D. & Neeckx, S. (eds) *Validation of wind turbine gearbox structural FE models through modal analysis at component and (sub-)assembly level.* (eds Desmet, W., Pluymes, B., Moens, D. & Neeckx, S.) *Proceedings of ISMA2022 International Conference on Noise and Vibration Engineering*, 4551–4565 (Leuven, 2022).

[18] Risaliti, E. *Model based virtual sensors for wheel center loads and full strain field on vehicle suspension components.* Ph.D. thesis, KU Leuven (2019).

[19] Vanhollebeke, F. *Dynamic Analysis of a Wind Turbine Gearbox Towards Prediction of Mechanical Tonalities.* Ph.D. thesis, KU Leuven (2015).